

---

This is an electronic reprint of the original article.  
This reprint may differ from the original in pagination and typographic detail.

Jin, Benjin; Wang, Qian; Sainio, Jani; Saveleva, Viktoriia A.; Jiang, Hua; Shi, Junjie; Ali, Basit; Kallio, Antti Jussi; Huotari, Simo; Sundholm, Dage; Han, Nana; Kallio, Tanja

## Amorphous carbon modulated-quantum dots NiO for efficient oxygen evolution in anion exchange membrane water electrolyzer

*Published in:*  
Applied Catalysis B: Environmental

*DOI:*  
[10.1016/j.apcatb.2024.124437](https://doi.org/10.1016/j.apcatb.2024.124437)

Published: 05/12/2024

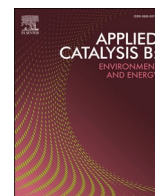
*Document Version*  
Publisher's PDF, also known as Version of record

*Published under the following license:*  
CC BY

*Please cite the original version:*  
Jin, B., Wang, Q., Sainio, J., Saveleva, V. A., Jiang, H., Shi, J., Ali, B., Kallio, A. J., Huotari, S., Sundholm, D., Han, N., & Kallio, T. (2024). Amorphous carbon modulated-quantum dots NiO for efficient oxygen evolution in anion exchange membrane water electrolyzer. *Applied Catalysis B: Environmental*, 358, Article 124437. <https://doi.org/10.1016/j.apcatb.2024.124437>

---

This material is protected by copyright and other intellectual property rights, and duplication or sale of all or part of any of the repository collections is not permitted, except that material may be duplicated by you for your research use or educational purposes in electronic or print form. You must obtain permission for any other use. Electronic or print copies may not be offered, whether for sale or otherwise to anyone who is not an authorised user.



## Amorphous carbon modulated-quantum dots NiO for efficient oxygen evolution in anion exchange membrane water electrolyzer

Benjin Jin<sup>a</sup>, Qian Wang<sup>b</sup>, Jani Sainio<sup>c</sup>, Viktoriia A. Saveleva<sup>d</sup>, Hua Jiang<sup>c</sup>, Junjie Shi<sup>a</sup>, Basit Ali<sup>a</sup>, Antti-Jussi Kallio<sup>e</sup>, Simo Huotari<sup>e</sup>, Dage Sundholm<sup>b</sup>, Nana Han<sup>a,\*</sup>, Tanja Kallio<sup>a,\*</sup>

<sup>a</sup> Department of Chemistry and Materials Science, School of Chemical Engineering, Aalto University, P.O. Box 16100, Aalto, FI-00076, Finland

<sup>b</sup> Department of Chemistry, Faculty of Science, University of Helsinki, P.O. Box 55, FI-00014, Finland

<sup>c</sup> Department of Applied Physics, School of Science, Aalto University, P.O. Box 15100, Aalto, FI-00076, Finland

<sup>d</sup> ESRF, The European Synchrotron, Grenoble 38043, France

<sup>e</sup> Department of Physics, University of Helsinki, P. O. Box 64, FI-00014, Finland

### ARTICLE INFO

#### Keywords:

Nickel oxide quantum dots  
Amorphous carbon nanosheets  
Oxygen Evolution Reaction  
Anion Exchange Membrane Electrolyzer  
High-valent Nickel

### ABSTRACT

Developing efficient electrocatalysts of elements that are abundant on earth crust is crucial for green hydrogen generation technologies. In particular, the oxygen evolution reaction (OER) under alkaline plays a key role in anion exchange membrane (AEM) electrolyzer to produce green hydrogen but suffers from low kinetic. Herein, nickel oxide quantum dots with highly uniform size distribution on ultrathin amorphous carbon nanosheets (NiO dots/a-carbon) were successfully prepared by a one-step method. Introducing NiO quantum dots onto amorphous carbon modifies the local coordination environment of Ni promoting it into a higher valence state. Benefitting from the promoted Ni<sup>δ+</sup> (2<δ<3) and the strong connection between Ni and amorphous carbon through Ni-O-C and Ni-C bonds, NiO dots/a-carbon exhibits excellent activity and stability towards OER in 0.1 M KOH using the rotating disk electrode. Moreover, a challenging current density of 500 mA cm<sup>-2</sup> is achieved at 1.7 V with a lab-scale AEM electrolyzer.

### 1. Introduction

Low temperature water electrolysis is a well-known technology enabling efficient storage of clean renewable energy into chemical bonds in the form of high-purity hydrogen [1,2]. Low temperature water electrolysis systems can be divided into the established alkaline electrolysis (AEL), demonstrated proton exchange membrane electrolysis (PEMEL), and emerging alkaline anion exchange membrane electrolysis (AEMEL) based on the electrolyte [3]. The PEMEL provides higher current density and energy efficiency than AEL and AEMEL because of a highly conductive and thin electrolyte [4]. However, the high loading of platinum group metals (PGM) and the expensive acid-tolerant stack hardware prevent it from becoming the governing electrolyzer technology [5]. In contrast, the primary advantage of AEL is the energy conversion based on earth abundant electrocatalysts rendering it as a sustainable technology for producing hydrogen up to megawatt scale [6–8].

Alkaline AEMEL offers the benefits of both AEL and PEMEL, achieving comparable performance while enabling utilization of PGM-

free catalysts [9,10]. In addition, AEMEL can be operated at different pressures with a reduced size and weight due to the membrane-based structure. The hydrocarbon membrane in alkaline AEMEL prefers the use of water or diluted alkaline solution (such as 0.1 M KOH) as the hydrogen source instead of a corrosive, concentrated alkaline electrolyte. The oxygen evolution reaction (OER) at the anode is one of the major energy-loss sources in AEMEL water electrolysis due to the slow kinetics and the high overpotential [11]. Thus, achieving an ideal OER performance with PGM-free catalysts in diluted alkaline solution is crucial, albeit challenging [12].

The nickel-based electrode is known as the most attractive anode material under alkaline conditions because of their large abundance on earth, outstanding catalytic performance, and stability to corrosion [13]. Considerable efforts have been devoted to increase the OER performance. Among them, construction of high-valent Ni species was considered as a desired means to activate nickel-based catalysts, however, it requires a high potential to achieve an excitation [14–16]. For example, NiFeCu oxyhydroxide catalysts were synthesized with the aim to create Ni<sup>3+</sup> sites that may improve the OER activity [17]. The desired

\* Corresponding authors.

E-mail addresses: [nana.han@aalto.fi](mailto:nana.han@aalto.fi) (N. Han), [tanja.kallio@aalto.fi](mailto:tanja.kallio@aalto.fi) (T. Kallio).

<https://doi.org/10.1016/j.apcatb.2024.124437>

Received 16 May 2024; Received in revised form 12 July 2024; Accepted 22 July 2024

Available online 22 July 2024

0926-3373/© 2024 The Author(s). Published by Elsevier B.V. This is an open access article under the CC BY license (<http://creativecommons.org/licenses/by/4.0/>).

$\text{Ni}^{3+}$  sites are generated by incorporating appropriate combinations of Cu. The prepared NiFeCu oxyhydroxide catalysts exhibit an excellent OER performance, with an overpotential of 385 mV at  $10 \text{ mA cm}^{-2}$  at pH = 7.2. Although the valence state of Ni can be promoted with redox metal doping, the definition of catalytic center remains controversial due to the collaborative catalysis caused by multi-active sites [18].

In addition to the embedding of redox metals, the incorporation with electron conducting non-metal supports could boost the catalytic performance, and this theory more than any other has motivated numerous structural and catalyst studies in the electrochemical field [19]. Several previous studies have been directed toward optimizing interactions between a chemically inert and large surface area possessing support and an active component [20,21]. A consensus has emerged that supports increase the dispersity of the active sites and thus facilitate mass transfer and electron transfer efficiency [22]. For example,  $\text{Co}_3\text{O}_4$  has been anchored on nitrogen-doped graphene to increase the OER activity. The increased activity of  $\text{Co}_3\text{O}_4/\text{N}$ -doped graphene is generally believed to arise from the synergetic effects between  $\text{Co}_3\text{O}_4$  and graphene [23]. However, a clear explanation of the synergetic catalytic mechanism is absent due to insufficient understanding of the role of non-metal supports in modulating the chemical properties of active components and the lack of suitable model materials.

In this work, uniformly distributed NiO quantum dots on ultrathin amorphous carbon (NiO dots/a-carbon) offers an exciting opportunity because of the simple chemical components and high density of active-site species. The unique two-dimensional (2D) nanostructures of amorphous carbon nanosheets is beneficial for stabilizing NiO quantum dots with a high surface energy. We demonstrate that the amorphous carbon not only increase the dispersity of the active sites but also modulates the valence state of nickel oxide. Introduction of amorphous carbon creates abundant oxygen functional groups with diverse coordination surroundings, which promotes the transformation of  $\text{Ni}^{2+}$  to  $\text{Ni}^{\delta+}$  ( $2 < \delta < 3$ ). The obtained NiO dots/a-carbon catalyst exhibits excellent catalytic activity towards OER in 0.1 M KOH, with an overpotential 296 mV at a current density of  $10 \text{ mA cm}^{-2}$ . A high current density of  $500 \text{ mA cm}^{-2}$  at 1.708 V is achieved with a lab-scale AEMEL, indicating highly efficient water splitting. Moreover, due to the strong interaction between amorphous carbon and nickel, the high valence state of  $\text{Ni}^{\delta+}$  ( $2 < \delta < 3$ ) is preserved even after a long-term operation of 10 000 cycles in a three-electrode measurement. In the alkaline AEMEL, the performance loss is negligible after a 12 h stability test at  $45^\circ\text{C}$  with a current density of  $500 \text{ mA cm}^{-2}$ .

## 2. Experimental section

### 2.1. Chemicals

Nickel acetylacetonate ( $\text{Ni}(\text{acac})_2$ , MW = 256.90 g/mol, 96 %) was purchased from Acros Organics. Lithium nitrate ( $\text{LiNO}_3$ ,  $M_r = 68.94 \text{ g/mol}$ ,  $\geq 98.0\%$ ) was purchased from Fluka. Nickel nitrate hexahydrate ( $\text{Ni}(\text{NO}_3)_2 \cdot 6 \text{ H}_2\text{O}$ ,  $M = 290.81 \text{ g/mol}$ ,  $\geq 99\%$ ) was purchased from Merck. Commercial  $\text{RuO}_2$  were purchased from Sigma and 5 wt% Nafion-117 solution was purchased from Aldrich. FAA-3-30 membrane and corresponding ionomer were purchased from Fumatech. All chemicals were used as received without further purification.

### 2.2. Synthesis of NiO dots/a-carbon and Nanocrystalline NiO

The NiO dots/a-carbon was synthesized using a salt template method [24,25]. In a typical process, 9 mg  $\text{Ni}(\text{acac})_2$ , 3 mg  $\text{Ni}(\text{NO}_3)_2 \cdot 6 \text{ H}_2\text{O}$  and 90 mg  $\text{LiNO}_3$  were ground together to obtain a mixed powder. The powder was then placed in an alumina boat and heated to the desired temperature (483 K) at a heating rate of 278 K/min in a tube furnace under flowing  $\text{N}_2$  gas with a speed of 50 mL/min. After holding the desired temperature for 2 h, the furnace was naturally cooled to room temperature to obtain the representative samples. The obtained

products were washed with DI water-ethanol mixture several times and dried in vacuum at 268 K overnight. Finally, the samples were stored in a glass vial for further using. Nanocrystalline NiO was synthesized with the same procedure but with a different annealing temperature (673 K).

### 2.3. Materials characterization

Transmission electron microscopy (TEM) images, high-angle annular dark-field scanning transmission electron microscopy (HAADF-STEM) images of all samples were recorded on JEOL JEM-2800 (Analytical HR-TEM) at 200 kV. Atomic resolution HAADF-STEM were taken using a JEOL2200FS, Cs-corrected HRTEM at an acceleration voltage of 200 kV. The atomic force image was carried out with a Bruker MultiMode 8. X-ray diffraction (XRD) patterns of samples were captured by PANalytical X'Pert Powder XRD operating at the voltage of 40 kV and a current of 40 mA with Cu  $K_\alpha$  radiation. X-ray photoelectron spectroscopy (XPS) was carried out with a Kratos Axis Ultra spectrometer using monochromated Al  $K_\alpha$  radiation, charge neutralization, a pass energy of 40 eV, an X-ray power of 75 W and an analysis area of roughly  $700 \mu\text{m} \times 300 \mu\text{m}$ . The binding energy scale was referenced to the O 1s peak of NiO at 529.3 eV. Atomic concentrations were determined from peak areas of high-resolution spectra after Shirley background subtraction using equipment specific sensitivity factors. The nickel  $2p_{3/2}$  peak was fitted with two peak envelopes corresponding to NiO and  $\beta$ -NiOOH. For a single peak envelope, only the intensity and full width at half maximum (FWHM) of the first peak was allowed to vary with all other peaks fixed relative to the first one. The binding energies of the first peaks were kept within  $\pm 0.1 \text{ eV}$  of literature values [26]. The carbon 1s peak was fitted in the same way with five components. An asymmetric peak shape was used for  $\text{sp}^2$  carbon and it was allowed to have a different FWHM than other carbon peaks. Ni  $K_\alpha$  high energy-resolution fluorescence-detected X-ray absorption near edge structure (HERFD--XANES) experiments were conducted at beamline ID26, European Synchrotron Radiation Facility (ESRF), Grenoble, France. The storage ring operated in 16 bunch mode with an electron current of 73 mA. The samples were analyzed, utilizing three undulators (u35) to produce incoming photons. A pair of cryogenically cooled Si(111) crystals then monochromatized the radiation. To calibrate the incident beam energy, a reference metallic iron foil set the first inflection point of the Ni K edge. In the experimental setup, Germanium Ge620 crystal analyzers in Rowland geometry were employed. Si avalanche photodiode (APD) with  $200 \mu\text{m}$  thickness and  $10 \times 10 \text{ mm}^2$  active area was used as a detector. The dead time correction was performed using a nonparalyzable model with  $\tau = 9.53 \cdot 10^{-8}$ . The data were collected in the presence of air at room temperature. HERFD XANES spectra were normalized by the incoming flux recorded by detecting the scattering from a Kapton foil with a photo diode and then were normalized in area using the full measured energy range. The data were collected at room temperature in fluorescence excitation mode. Before the synchrotron XAS measurements, we performed laboratory-scale XANES analyses using the Helsinki Center for X-ray Spectroscopy of the University of Helsinki. The x-rays from a conventional water-cooled Ag anode x-ray tube (20 kV/40 mA) were monochromated with a Johann-type Si(551) spherically bent crystal analyzer, curvature radius  $R=0.5 \text{ m}$ , and detected by a silicon drift diode.

### 2.4. Electrochemical measurements

The electrochemical experiments were performed in a standard three-electrode cell using an Autolab potentiostat (PGSTAT128N, Metrohm Autolab B.V.) equipped with a rotating disk electrode (RDE) system (Pine Instrument) at room temperature. A 0.1 M KOH solution was used as electrolyte. A commercial Hg/HgO electrode and a graphite rod were used as a reference and counter electrode, respectively. Samples were studied using a glassy carbon electrode (GCE, 5 mm diameter,  $0.196 \text{ cm}^2$ ) as a working electrode. The GC tip was pre-polished with

50 nm alumina slurry and sonicated in ultrapure H<sub>2</sub>O and ethanol for 3 mins. A catalyst ink was prepared by dispersing 4 mg catalyst and 2.0 mg carbon black (Vulcan XC-72, VC) in 1000  $\mu$ l solution containing 970  $\mu$ l isopropanol and 30  $\mu$ l Nafion solution. The catalyst ink was then ultrasonicated and stirred overnight to form a homogeneous ink. The well-dispersed ink (10  $\mu$ l) was drop casted onto the GC electrode while drying naturally yielding a total mass loading of 204  $\mu$ g<sub>cat</sub> cm<sup>-2</sup>. Commercial RuO<sub>2</sub> samples were prepared with the same method. The cyclic voltammetry (CV) with a scan rate of 100 mV s<sup>-1</sup> were first employed until the CV was overlapping. The OER performances of the catalysts were assessed by performing linear sweep voltammetry (LSV) at a scan rate of 5 mV s<sup>-1</sup> with a rotation speed of 1600 rpm. The onset potential is defined as the potential at current density of 1.5 mA cm<sup>-2</sup>. The electrochemical impedance spectroscopy (EIS) was performed at 1.6 V with respect to reversible hydrogen electrode (RHE) with an amplitude of 5 mV from 100 kHz to 0.1 Hz. Cyclic voltammetry measurements were carried out with an increasing scan rate from 20 to 120 mV s<sup>-1</sup> to evaluate the double-layer capacitance (C<sub>dl</sub>). Electrochemically active surface area (ECSA) was estimated according to the equation: ECSA = C<sub>dl</sub>/C<sub>s</sub> × A<sub>geometric</sub>, C<sub>s</sub> = 0.04 mF cm<sup>-2</sup>. The measured potentials were calibrated to the RHE by the following equation: E<sub>RHE</sub> = E<sub>Hg/HgO</sub> + 0.098 V + 0.059 × pH. A lower loading of the catalyst was used for the rotating ring-disk electrode (RRDE) to limit the number of oxygen bubbles which may reduce the collection efficiency of the Pt ring [27]. The Faradaic efficiency ( $\epsilon$ ) was calculated using the equation  $\epsilon = 100\% \times j_{ring} / (N \times j_{disk})$ , where  $j_{disk}$  is the disk current density,  $j_{ring}$  is the ring current density and  $N$  is the collection efficiency (38.3 %) of the RRDE. The accelerated durability tests (ADT) of the catalysts were assessed by CV at a scan rate of 100 mV s<sup>-1</sup> between 1.2 and 1.65 V with respect to RHE for 10 000 continuous cycles.

## 2.5. Electrochemical measurements for water electrolyzer

The electrolyser setup consists of a circular shape cell that has anode and cathode compartments separated by a membrane electrode assembly (MEA). 0.1 M KOH is circulated in both compartments at 60 mL/min. The compartments consist of a titanium piston, a titanium mesh, and a titanium sinter. The MEA is placed between the sinters and the two sides are closed by tightening four screws to a torque of 1.5 Nm. To ensure a proper electrical contact between the cell parts, technical grade N<sub>2</sub> is applied to titanium pistons at 10 bar. The circulated 0.1 M KOH is heated by heat exchangers before entering the anode/cathode compartments. The cell temperature is measured at the outlet of 0.1 M KOH solution, which is set at 45 °C. The cell measurements were conducted using an AUTOLAB PGSTAT302N potentiostat equipped with a Booster 20 A and a Nova 2.1 software. The cell was left to stabilize for 2 h before starting the measurements. The anode ink was prepared by adding a certain amount of NiO dots/a-carbon or commercial RuO<sub>2</sub> with 30 wt% ionomer solution (5 wt% Fumion FAA-3 in ethanol, Fumatech) into a mixed solution of water and isopropanol. The ink was then sonicated and stirred until the ink was homogeneous. The cathode ink was prepared with commercial PtRuC using the same procedure. The catalyst was deposited onto the membrane using an airbrush with nitrogen flow. Finally, the MEA was pressed with 5 metric tons at room temperature for 120 s. The voltage-current polarization curves were obtained at a scan rate of 5 mV s<sup>-1</sup>. The durability test of the OER was carried out at 500 mA cm<sup>-2</sup> and the EIS measurements at voltage of 1.6 V from 10 kHz to 0.1 Hz with an amplitude of 8 mV.

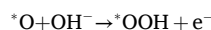
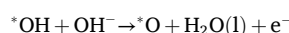
## 2.6. Computational details

Spin-polarized density functional theory (DFT) calculations were performed with the VASP program package at the generalized gradient approximation (GGA) using the Perdew–Burke–Ernzerhofer (PBE) functional [28–31]. The interactions between ions and electrons were calculated by the projector augmented wave (PAW) method [32,33].

The Hubbard-corrected density-functional theory (DFT + U) approach was used to correct for the self-interaction error [34]. Hund's exchange coupling was also considered by using a U-J parameter of 5.3 eV for Ni [35,36]. The van der Waals (vdW) interactions were accounted for with the semi-empirical D3 correction [37]. An accurate cubic NiO unit cell as well as its electronic structure were obtained by sampling the Brillouin zone with a k-point mesh. The kinetic-energy cutoff was set to 500 eV in the plane-wave expansion.

Based on the experimental X-ray diffraction (XRD) data, we investigated the (200) plane since it is the most exposed surface. A unit cell with four slab layers of  $\sim 10$  Å was used to ensure enough space for the adsorption. The two lower layers representing cubic NiO are frozen while the upper layers are allowed to relax to simulate the surface. The distance between neighboring slab groups is 15 Å to avoid significant interaction between layers. A NiO surface and a singly oxidized NiO surface representing high-valence NiO surfaces were constructed. In the electronic structure studies, we increased the k-point values of the surface to 5x5x1, whereas the structure optimizations were performed with 3x3x1 k-point values. The convergence criteria of the total energy and the forces in the structure optimization were set to 10<sup>-5</sup> eV and 0.02 eV/Å, respectively.

The oxygen evolution reaction (OER) is a four-step reaction which includes transfer of four electrons:



where \* stands for an active site on the surface. \*OH, \*O and \*OOH are adsorbed intermediates. The change in Gibbs free energy ( $\Delta G$ ) is obtained from the change in the electronic energy ( $\Delta E$ ), the vibrational zero-point energy correction ( $\Delta E_{\text{ZPE}}$ ), the entropy contribution ( $T\Delta S$ ) and the pH contribution to Gibbs free energy.

$$\Delta G = \Delta E + \Delta E_{\text{ZPE}} - T\Delta S + \Delta G(\text{pH})$$

T is temperature and S is entropy. Since the reactants leave either as adsorbed species or as liquid, the entropy is assumed to be constant ( $T\Delta S = 0$ ). The pH contribution to Gibbs free energy at a pH of 13 can be estimated using  $\Delta G(\text{pH}) = k_{\text{B}}T \times \text{pH} \times \ln 10 = 0.059 \times 13 = 0.767 \text{ eV}$ , when T is 298 K and  $k_{\text{B}}$  is Boltzmann's constant. The  $\Delta G(\text{OH})$  change in the Gibbs free energy is obtained as

$$\Delta G(\text{OH}) = G(\text{H}_2\text{O}) - \frac{1}{2}G(\text{H}_2)$$

The free energy for each OER step is then given by

$$G_1 = G(*\text{OH}) - G(\text{OH}) - G(*) \rightarrow \Delta G_1 = G_1 - eU + 0.767$$

$$G_2 = G(*\text{H}_2\text{O}) + G(\text{O}) - G(\text{OH}) - G(*\text{OH}) \rightarrow \Delta G_2 = G_2 - G_1 - eU + 0.767$$

$$G_3 = G(-G(\text{OH}) - G(*\text{O})) \rightarrow \Delta G_3 = G_3 - G_2 - eU + 0.767$$

$$\Delta G_4 = 4.92 - (\Delta G_1 + \Delta G_2 + \Delta G_3) - eU + 0.767$$

The overpotential ( $\eta$ ) is defined as  $\eta = \max\{\Delta G_1, \Delta G_2, \Delta G_3, \Delta G_4\}$ .

## 3. Results and discussion

### 3.1. Synthesis and structure characterization of NiO dots/a-carbon

The NiO dots/a-carbon was synthesized by mixing nickel (II) acetylacetonate (Ni(acac)<sub>2</sub>), nickel nitrate hexahydrate and lithium nitrate (LiNO<sub>3</sub>) at a mass ratio of 3:1:30 by grinding. The mixture was then transferred into a tube furnace, where it was annealed at 483 K for 2 h under a nitrogen flow. After cooled down to room temperature NiO

dots/a-carbon was obtained by removing  $\text{LiNO}_3$  by washing and centrifugation. The synthesis yielded uniform NiO quantum dots distributed on amorphous carbon.

The morphological and structural characteristics of NiO dots/a-carbon is illustrated in Fig. 1. The transmission electron microscopy (TEM) image shows the typical two-dimensional morphology of NiO dots/a-carbon while the wrinkles and undulating surface indicate the ultrathin feature of NiO dots/a-carbon (Fig. 1a and Fig. 1b). The high-resolution transmission electron microscopy (HR-TEM) image in Fig. 1c reveals that the ultrathin 2D structure consists of extremely tiny nanoparticles. The high angle annular dark-field scanning TEM (HAADF-STEM) image reveals that the ultrafine NiO quantum dots are well distributed (Fig. 1d). Furthermore, the NiO dots have a uniform size distribution with an average diameter of  $1.2 \pm 0.1$  nm based on statistical analysis in Fig. S1. The atomic resolution HAADF-STEM image in Fig. 1e clearly shows lattice fringes with 0.21 nm, which is consistent with the (012) plane distance of NiO. It is worth noting that the surfaces of the NiO quantum dots expose numerous disorder atoms and the NiO may overlap due to high quantum dots density. The atomic force microscopy (AFM) image demonstrates the ultrathin 2D structure with a thickness around 2 nm (Fig. 1f). A Raman spectrum is recorded to investigate the structure of the carbon support (Fig. S2). Two typical peaks of carbon materials can be observed for both NiO dots/a-carbon and commercial graphite, namely, the  $I_D$  peak (disorder) at  $1360\text{ cm}^{-1}$  and the  $I_G$  peak (graphite) at  $1580\text{ cm}^{-1}$ . Compared with commercial graphite, the broader  $I_D$  and  $I_G$  peaks of NiO dots/a-carbon are caused by the disordered carbon structure and the presence of NiO dots [38,39]. Control experiments were carried out to investigate the growth process, which reveals that the formation of the ultrathin 2D structure highly depend on the temperature. At a lower temperature of 453 K a 3D bending structure is formed (Fig. S3), while the nanocrystalline NiO counterpart (Fig. S4) is obtained at a higher temperature (673 K). The NiO quantum dots can be produced with only one Ni source, nickel (II) acetylacetonate, but that yields lower Ni loading (Fig. S3). Hence, Ni ( $\text{NO}_3$ )<sub>2</sub> is used as an additional Ni source to increase the Ni loading. In the X-ray diffraction (XRD) pattern shown in Fig. 1g, nanocrystalline NiO exhibits sharp peaks at  $2\theta = 36.9^\circ, 42.8^\circ, 62.2^\circ, 74.6^\circ$  and  $78.5^\circ$ , which can be assigned to NiO (PDF # 47-1049). NiO dots/a-carbon displays a group of broadened peaks compared to nanocrystalline NiO. This difference can be attributed to the tiny particle size of the NiO dots. The selected area electron diffraction (SAED) pattern in Fig. 1h consists of concentric rings, which indicate the polycrystalline nature of NiO dots/a-carbon. The interplanar spacing and lattice parameters that have been calculated using the measured radius of each diffraction ring match well with the XRD analysis. The HAADF-STEM image and the corresponding energy-dispersive X-ray spectroscopy (STEM-EDS) elemental mapping (Fig. 1i) indicate that C, O and Ni are homogeneously distributed. A higher concentration of C, O and Ni can be observed in the marked circles, which is caused by the overlapping of carbon nano-sheets. The semi-quantitative EDS spectrum (Fig. S5) reveals that the overall elemental composition of NiO dots/a-carbon is 38/46/16 (Ni/O/C).

### 3.2. Amorphous carbon modification for NiO quantum dots

The chemical composition and valence state of the NiO dots/a-carbon of the nanocrystalline NiO catalysts were investigated by X-ray photoelectron spectra (XPS). The survey spectra analysis in Fig. S6 confirms that Ni, O, and C elements exist in both materials. Fig. 2a shows that the Ni 2p region of the Ni compounds have a complex peak shape resulting from multiple splitting as well as from shake-up and plasmon loss structures. The sharp peak observed around 853.7 eV is a NiO signature, which is clearly present in both samples. The  $2p_{3/2}$  peaks have been fitted with two peak envelopes, one for NiO and another for  $\beta\text{-NiOOH}$ , producing a reasonable fit to the data. The assignment to  $\beta\text{-NiOOH}$  is based on parameters and peak shapes given in M. C.

Biesinger' work [26,40]. However, somewhat tentative since the peak shapes of other nickel compounds resemble closely the one of  $\beta\text{-NiOOH}$  [26,40]. The amount of  $\beta\text{-NiOOH}$  is estimated to be  $11\% \pm 2\%$  and  $21\% \pm 4\%$  (error bars obtained by varying background and fitting parameters) of all Ni of nanocrystalline NiO and NiO dots/a-carbon, respectively. The observed increase in the  $\beta\text{-NiOOH}/\text{NiO}$  ratio suggests that NiO dots/a-carbon possesses a higher oxidation state of Ni. Previous reports demonstrated that high-valent Ni sites in NiOOH promote the energy band of O atoms near the Fermi level, thus activating lattice O sites [41,42]. The O 1s region in Fig. S7 shows a lattice oxygen peak related to NiO at 529.3 eV and another broader peak roughly at 531.3 eV. The higher binding energy peak can be due to defective sites in NiO and/or hydroxides but especially in the NiO dots/a-carbon sample also due to the presence of different carbon-oxygen bonds [26]. The peaks related to O-C=O bonds ( $\sim 289.8$  eV), C=O bonds ( $\sim 288.3$  eV), C-OH/C-O-C bonds ( $\sim 286.5$  eV),  $\text{sp}^3$  carbon bonds ( $\sim 285.0$  eV) and  $\text{sp}^2$  carbon bonds ( $\sim 284.5$  eV) have been fitted in the C 1s region (Fig. 2b) [40,43]. The nanocrystalline NiO sample shows mainly  $\text{sp}^3$  and C=O bonds, whereas in NiO dots/a-carbon also  $\text{sp}^2$ , C-OH/C-O-C and O-C=O bonds are observed. The atomic percentages of the elements for nanocrystalline NiO and NiO dots/a-carbon including peak fitting results are shown in Table S1. The Fourier transform infrared spectroscopy (FTIR) was used to obtain information about the carbon-oxygen bonds. Fig. 2c shows that the peaks corresponding to the C=C stretching mode, at  $1580\text{ cm}^{-1}$  and  $1515\text{ cm}^{-1}$  and the C-O stretching mode, at  $1270\text{ cm}^{-1}$  are present only in the IR spectrum of NiO dots/a-carbon, which is consistent with the XPS analysis [44]. The functional groups introduced by the amorphous carbon provide diverse coordination sites for nickel.

To further investigate the coordination environments of NiO dots/a-carbon, we used X-ray absorption spectroscopy (XAS) characterization. Fig. 2d and Fig. S8 show the normalized Ni K-edge XANES spectra of the commercial NiO nanoparticles (NiO NPs), nanocrystalline NiO and NiO dots/a-carbon. The Ni K-edge XANES spectrum consists of three parts, the pre-edge, the rising-edge, and the white line. The pre-edge peak is located on the low-energy side at 8332 eV, which is considered as the transition from Ni 1s state to the mixed states of Ni 3d with O 2p [45, 46]. The intensity of the pre-edge peak correlates with various factors, such as the magnitude of hybridization of the Ni 3d and O 2p, the amount of the  $3d^8L$  configuration and holes in O 2p states in the ground state, and the Ni-O bond length in different samples [45,47]. The pre-edge intensity in NiO dots/a-carbon is lower than in nanocrystalline and commercial NiO NPs, which can be explained by the Zaanen-Sawatzky-Allen model [48]. One reason is that the structure of NiO dots/a-carbon is more disordered compared to crystalline NiO. This increased disorder reduces the overlap between Ni 3d and O 2p orbitals, thus decreasing the hybridization. Another possible reason is that the increase of the Ni-O charge transfer energy accompanied by a reduced number of ground state configurations with holes in the O 2p states weaken the transition from Ni 1s to unfilled levels. Thus, the lower intensity of the pre-edge peak in NiO/a-carbon can be associated with the disordered structure of NiO dots/a-carbon and the less covalent Ni-O bond. Compared to nanocrystalline NiO and commercial NiO NPs, the absorption edge of NiO dots/a-carbon is shifted to higher energies, revealing the increase of the Ni oxidation state in NiO dots/a-carbon, which is in line with the XPS results [49]. The white line peak of the Ni K-edge spectrum at 8350 eV belongs to the electronic transition from Ni 1s to the unoccupied 4p orbital [13]. The white line intensity in NiO dots/a-carbon is higher than nanocrystalline and commercial NiO NPs, indicating higher valence state of Ni in NiO dots/a-carbon [13,50]. The  $k$ -space oscillations of NiO dots/a-carbon are lower in intensity and gradually weaken compared to those of nanocrystalline NiO in Fig. S9, indicating a disordered structure of NiO dots/a-carbon. In the  $R$ -space spectra (Fig. 2e), nanocrystalline NiO shows two main peaks corresponding to the Ni-O and Ni-Ni coordination shells, respectively. The extended X-ray absorption fine structure (EXAFS) structural fitting was

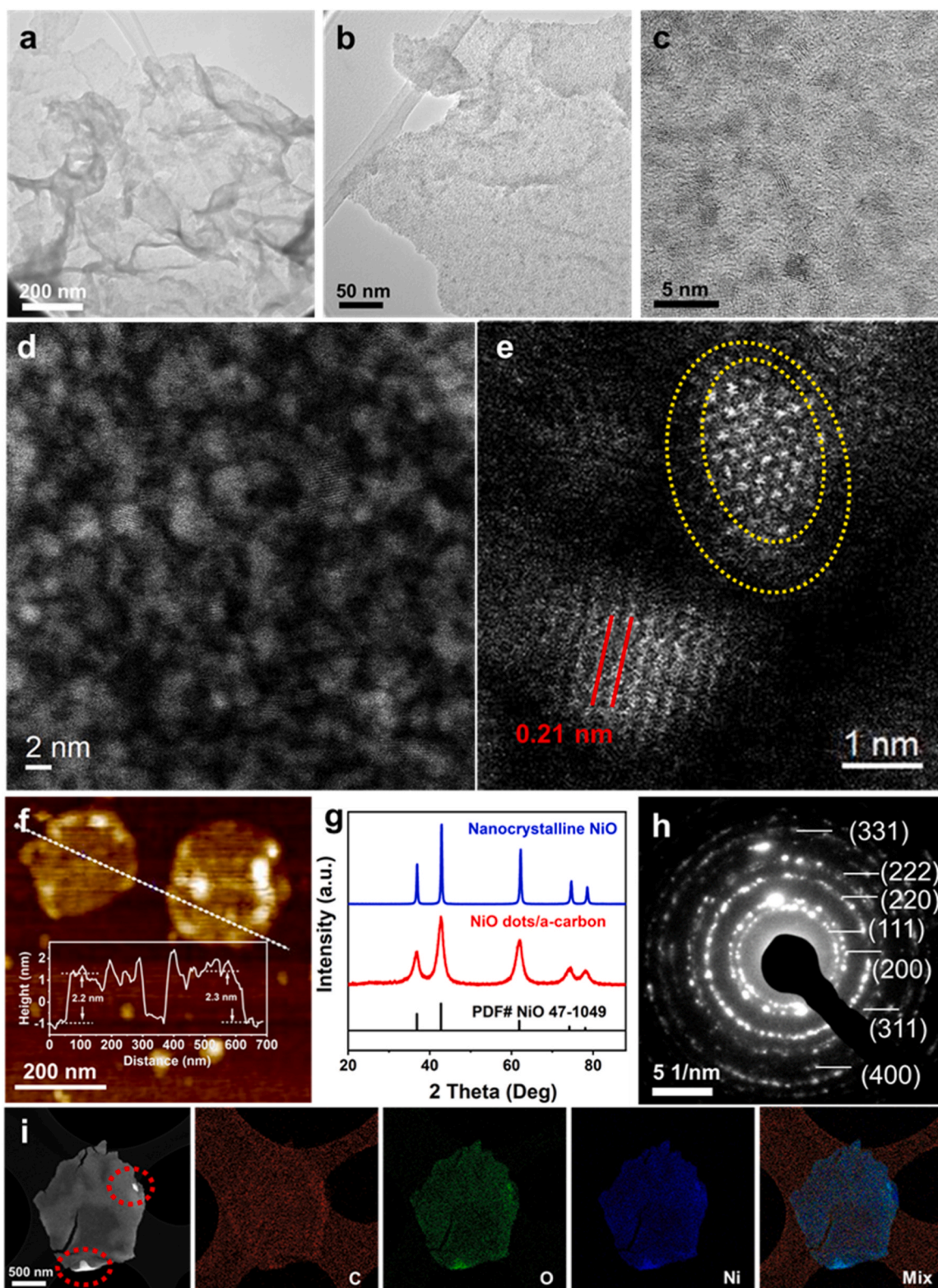


**Fig. 1.** Structure Characterization of NiO dots/a-carbon. a) and b) The TEM images of NiO dots/a-carbon. c) A HR-TEM image of NiO dots/a-carbon. d) An HAADF-STEM image and e) an atomic resolution HAADF-STEM image of NiO dots/a-carbon. The gap between yellow circle represents disorder. f) An AFM image and height profile of NiO dots/a-carbon. g) XRD pattern of NiO dots/a-carbon and nanocrystalline NiO. h) SAED pattern of NiO dots/a-carbon. i) An HAADF-STEM image of NiO dots/a-carbon and the corresponding STEM-EDX elemental mapping of C, O, Ni, and the mixture of C, O and Ni elements.

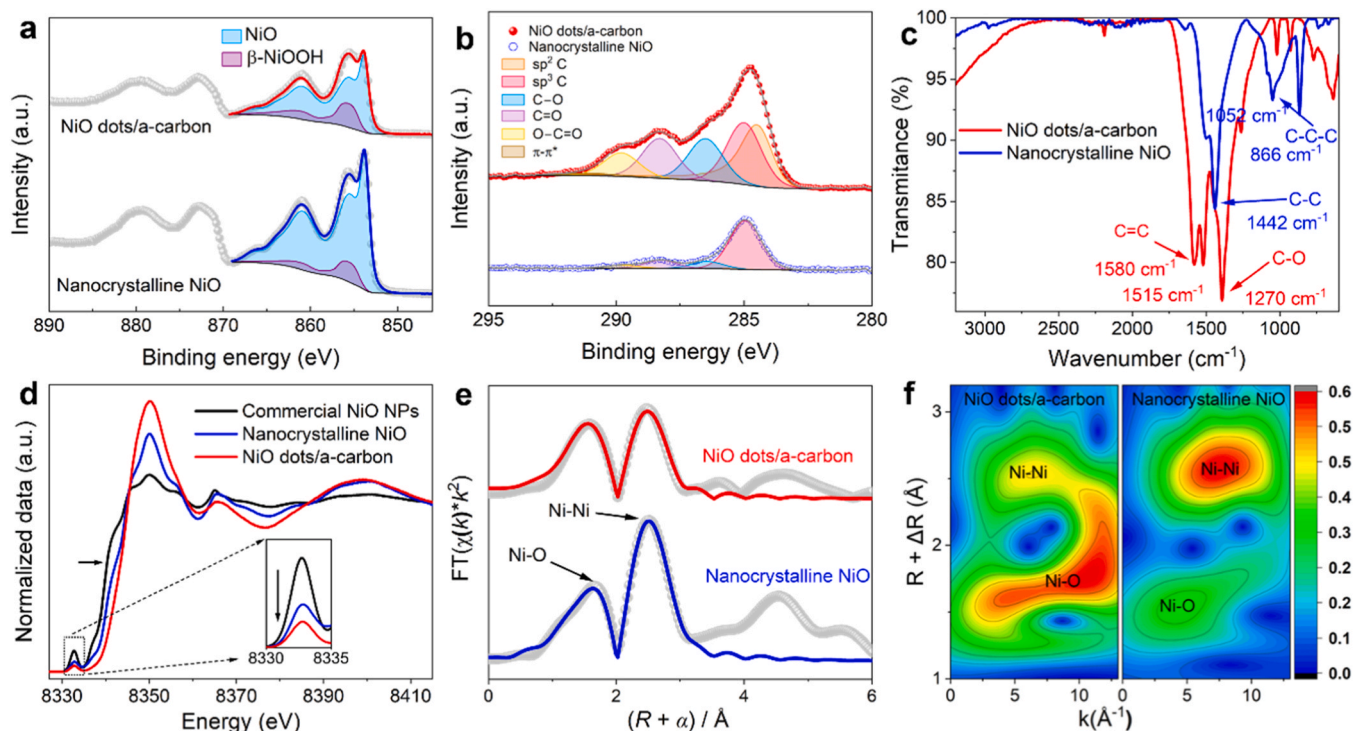


**Fig. 2.** Structure Characterization of NiO dots/a-carbon. XPS spectra of a) Ni 2p and b) C 1s of the nanocrystalline NiO and NiO dots/a-carbon. c) The FT-IR spectrum of nanocrystalline NiO and NiO dots/a-carbon. d) The Ni K-edge XANES spectra of commercial NiO nanoparticles, nanocrystalline NiO and NiO dots/a-carbon. e) The  $k^2$ -weighted  $\chi(k)$ -function of the EXAFS spectra of nanocrystalline NiO and NiO dots/a-carbon. f) The wavelet transforms of the Ni K-edge EXAFS data of nanocrystalline NiO and NiO dots/a-carbon.

implemented with Ni-O and Ni-Ni paths for both NiO dots/a-carbon and nanocrystalline NiO. The coordination number of Ni-O ( $N_{\text{Ni-O}}$ ) in NiO dots/a-carbon ( $N_{\text{Ni-O}} = 5.0$ ) is smaller than for nanocrystalline NiO ( $N_{\text{Ni-O}} = 4.7$ ) as shown by the fitting parameters in Table S2. Meanwhile, the coordination numbers of the Ni-Ni shell ( $N_{\text{Ni-Ni}}$ ) in NiO dots/a-carbon ( $N_{\text{Ni-Ni}} = 8.8$ ) are much lower than that of nanocrystalline NiO ( $N_{\text{Ni-Ni}} = 11.0$ ). It is noted that attributing the first coordination shell to pure Ni-O in NiO dots/a-carbon is debatable because of the abundant coordination sites and the diverse coordination environments provided by amorphous carbon. The wavelet transform of the Ni K-edge EXAFS spectrum (Fig. 2f) in NiO dots/a-carbon shows lateral broadening in the imaginary part compared with nanocrystalline NiO, suggesting a more complex coordination of Ni in the first shell.

### 3.3. OER performance of NiO dots/a-carbon

The electrocatalytic OER performance of NiO dots/a-carbon, nanocrystalline NiO and commercial RuO<sub>2</sub> were evaluated in 0.1 M KOH at room temperature. The average size of commercial RuO<sub>2</sub> is  $34 \pm 5$  nm based on a statistical analysis of 50 nanoparticles (Fig. S11). The cyclic voltammetry (CV) was performed for NiO dots/a-carbon and nanocrystalline NiO at a scan rate of  $100 \text{ mV} \cdot \text{s}^{-1}$  until a stable signal is obtained. Fig. S12 shows that one broad peak at around  $1.37 V_{\text{RHE}}$  belonging to Ni (II/III) redox reactions appear for both catalysts [51]. An obvious negative shift in the peak potential ( $E_p$ ) and an increase in the peak current density ( $I_p$ ) can be observed with increase in cycling numbers for the NiO dots/a-carbon catalysts. The negative shift of  $E_p$  indicates more efficient OER and an increased  $I_p$  is related to a higher exposed area, which are signatures of an efficient OER catalysts. The redox peak differences in nanocrystalline NiO are negligible compare with NiO dots/a-carbon.

In Fig. 3a, NiO dots/a-carbon exhibits a more negative onset potential of  $1.47 V_{\text{RHE}}$  than nanocrystalline NiO ( $1.54 V_{\text{RHE}}$ ) and commercial RuO<sub>2</sub> ( $1.51 V_{\text{RHE}}$ ). To generate a current density of  $10 \text{ mA cm}^{-2}$ ,

NiO dots/a-carbon needs an overpotential of 296 mV, while nanocrystalline NiO and commercial RuO<sub>2</sub> require a higher overpotential of 365 mV and 410 mV, respectively (Fig. 3b). For a full comparison, NiO dots were well deposited on Vulcan carbon and Kuraray carbon by impregnation and subsequent pyrolysis process (Fig. S13), and the OER activity were measured under the same conditions. The linear sweep voltammetry (LSV) of NiO dots/a-carbon, NiO dots/Kuraray carbon and NiO dots/Vulcan carbon is shown in Fig. S14. NiO dots/Kuraray carbon and NiO dots/Vulcan carbon require an overpotential of 361 mV and 401 mV to achieve a current density of  $10 \text{ mA cm}^{-2}$ , which are 65 and 105 mV higher than for NiO dots/a-carbon catalysts. Fig. S15 reveals that the OER activity of the pure carbon support is negligible. These results indicate that the NiO is more efficient for OER on amorphous carbon than on the Vulcan or Kuraray carbon.

The Tafel slope of NiO dots/a-carbon in Fig. 3c is  $51 \text{ mV dec}^{-1}$  which differs from that of nanocrystalline NiO ( $73 \text{ mV dec}^{-1}$ ) and commercial RuO<sub>2</sub> ( $161 \text{ mV dec}^{-1}$ ), suggesting that the rate-determining step (RDS) for NiO dots/a-carbon, nanocrystalline NiO and commercial RuO<sub>2</sub> are  $\text{OOH}_{\text{ads}}$  formation (step III), deprotonation of adsorbed OH into  $\text{O}_{\text{ads}}$  (step II), and the initial  $\text{OH}_{\text{ads}}$  formation (step I), respectively [52]. The combined merits of NiO dots/a-carbon including the overpotentials and Tafel slopes (Fig. 3d), are superior to the most reported non-noble OER catalysts (Table S3) [53–63].

The electrochemical active surface area (ECSAs) is evaluated by double-layer capacitance ( $C_{\text{dl}}$ ) measurements (Fig. S16). NiO dots/a-carbon displays a  $C_{\text{dl}}$  of  $3.5 \text{ mF cm}^{-2}$ , which is larger than that of nanocrystalline NiO ( $2.5 \text{ mF cm}^{-2}$ ) and smaller than for commercial RuO<sub>2</sub> ( $7.4 \text{ mF cm}^{-2}$ ), suggesting that the exposed active surface area of NiO dots/a-carbon is larger than for nanocrystalline NiO (Fig. 3e). Fig. S17 indicates that the contributions of carbon support to  $C_{\text{dl}}$  is  $0.31 \text{ mF cm}^{-2}$ , which is an order of magnitude smaller compared with the metal catalysts. The LSV data normalized by ECSA shown in Fig. 3f provides information about the intrinsic activity. NiO dots/a-carbon exhibits high performance after ECSA normalization, indicating that

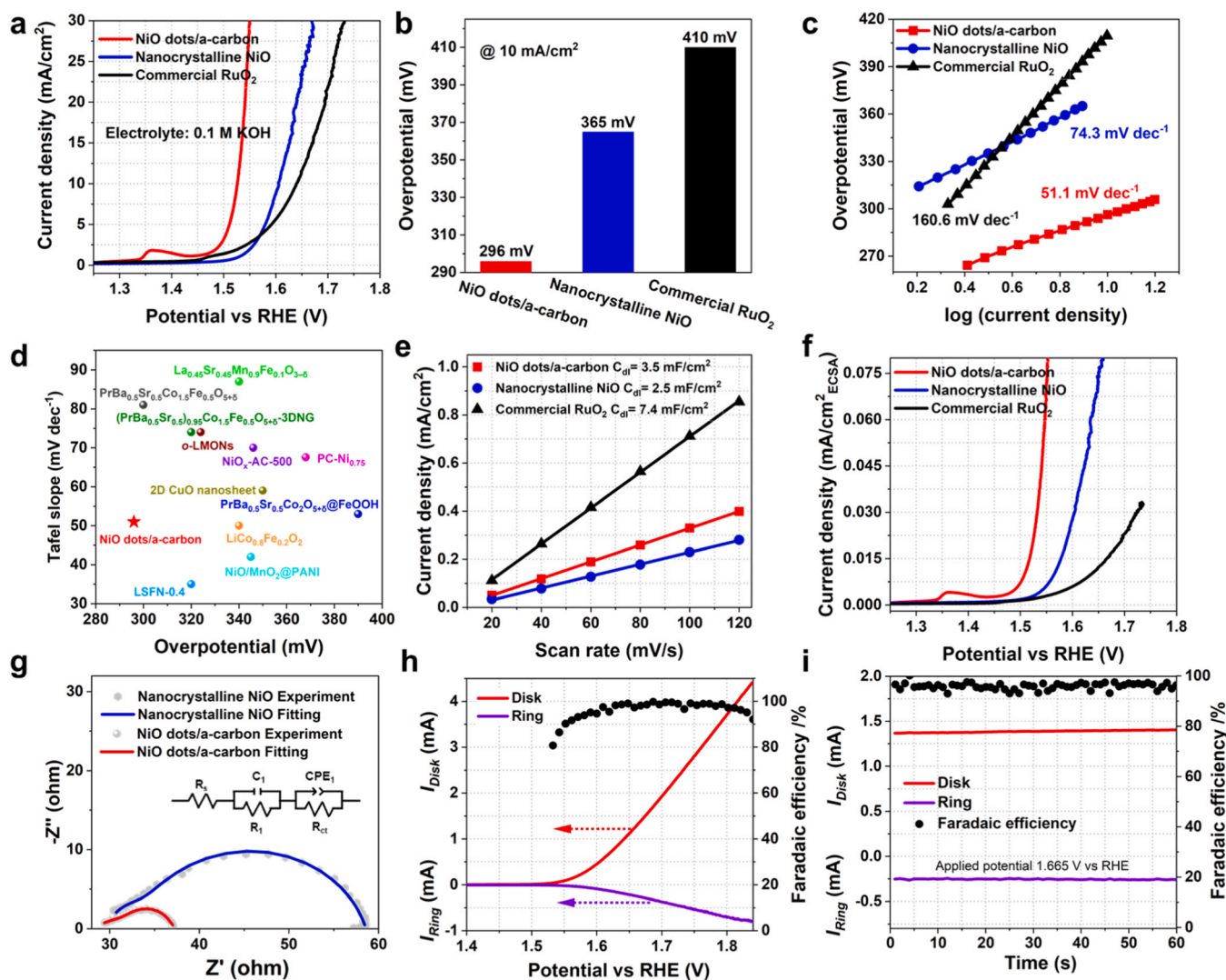


**Fig. 3.** OER activity characterization. a) The OER polarization curves, b) overpotentials at a current density of  $10 \text{ mA cm}^{-2}$  and c) Tafel slopes of NiO dots/a-carbon, nanocrystalline NiO and commercial  $\text{RuO}_2$ . e) The double-layer capacitances ( $C_{dl}$ ) and f) the ECSA normalized polarization curves of NiO dots/a-carbon, nanocrystalline NiO and commercial  $\text{RuO}_2$ . d) The Comparison of merit with respect to both Tafel slope and the overpotential at  $10 \text{ mA cm}^{-2}$ . g) Nyquist plots and fitted equivalent circuit of NiO dots/a-carbon and nanocrystalline NiO. The  $R_s$ ,  $R_{ct}$ , and  $CPE_1$  are the ohmic resistances, charge transfer resistance and constant phase element representing the double layer capacitance, respectively. h) The Linear sweep rotating ring-disk electrode (RRDE) of NiO dots/a-carbon. i) The potentiostatic-RRDE of the NiO dots/a-carbon catalyst.

its intrinsic activity is excellent. Nyquist plots and the fitted equivalent circuit of NiO dots/a-carbon and nanocrystalline NiO are shown in Fig. 3g and Table S4. The high frequency region ( $R_1C_1$ ) circuit represents the diffusion/adsorption process of the reaction intermediates due to slow diffusion through the reaction interface [64]. The NiO dots/a-carbon has the lowest charge-transfer resistance ( $R_{ct} = 5.8 \Omega$ ) as compared to nanocrystalline NiO ( $R_{ct} = 25.5 \Omega$ ) and commercial  $\text{RuO}_2$  ( $R_{ct} = 33.8 \Omega$ , Fig. S18), indicating that the kinetics of the NiO dots/a-carbon samples is improved [65]. The  $C_{dl}$  calculated from the fitted  $CPE_1$  obtained using electrochemical impedance spectroscopy (EIS) analysis are  $6.5 \text{ mF cm}^{-2}$  and  $2.5 \text{ mF cm}^{-2}$  for NiO dots/a-carbon and nanocrystalline NiO, respectively, which is in line with the value evaluated from cyclic voltammetry (CV) measurements.

The rotating ring-disk electrode (RRDE) measurements were carried out to evaluate the Faradaic efficiency of OER in  $\text{O}_2$ -saturated  $0.1 \text{ M KOH}$ . Fig. 3h shows LSV data with calculated Faradaic efficiency for the NiO dots/a-carbon catalysts. The Faradaic efficiency was calculated at  $1.58 \text{ V}_{\text{RHE}}$  because pseudocapacitive currents contribute significantly to the obtained currents in the low potential region [27]. The Faradaic efficiency is close to 100 % between  $1.65 \text{ V}_{\text{RHE}}$  and  $1.8 \text{ V}_{\text{RHE}}$ , suggesting

that the oxidation current can be attributed to OER through a four-electron transfer pathway. The Faradaic efficiency shows a slight decrease after  $1.8 \text{ V}_{\text{RHE}}$ , due to the decrease in the collection efficiency of the RRDE resulting from the formation of oxygen bubbles adhered to the electrode surface. Potentiostatic-RRDE measurements are reported in Fig. 3i. The measurements show that there is a very small change in Faradic efficiency when using  $1.665 \text{ V}_{\text{RHE}}$  for 60 s.

Stability is another critical condition for evaluating the performance of OER electrocatalysts (Fig. 4). The chronopotentiometry curve of NiO dots/a-carbon shown in Fig. 4a with a current density of  $10 \text{ mA cm}^{-2}$  demonstrates that the electrode operates well for 25 h. The discontinuities observed at 2.5 h and 6 h are plausibly due to poor wetting of NiO dots/a-carbon at the beginning of measurements. The evolved hydrophobic oxygen gas adheres on the poorly wetted surfaces, blocking active sites and leading to intermittent performance drops. Once the bubbles grow large enough to detach, the performance recovers, contributing to the discontinuous pattern. Besides, NiO dots/a-carbon (Fig. 4b) exhibits merely a 7 mV voltage loss after 10 000 cycles in accelerated deterioration tests (ADT) in  $\text{N}_2$ -saturated  $0.1 \text{ M KOH}$ , indicating its high durability. Contrary, the nanocrystalline NiO

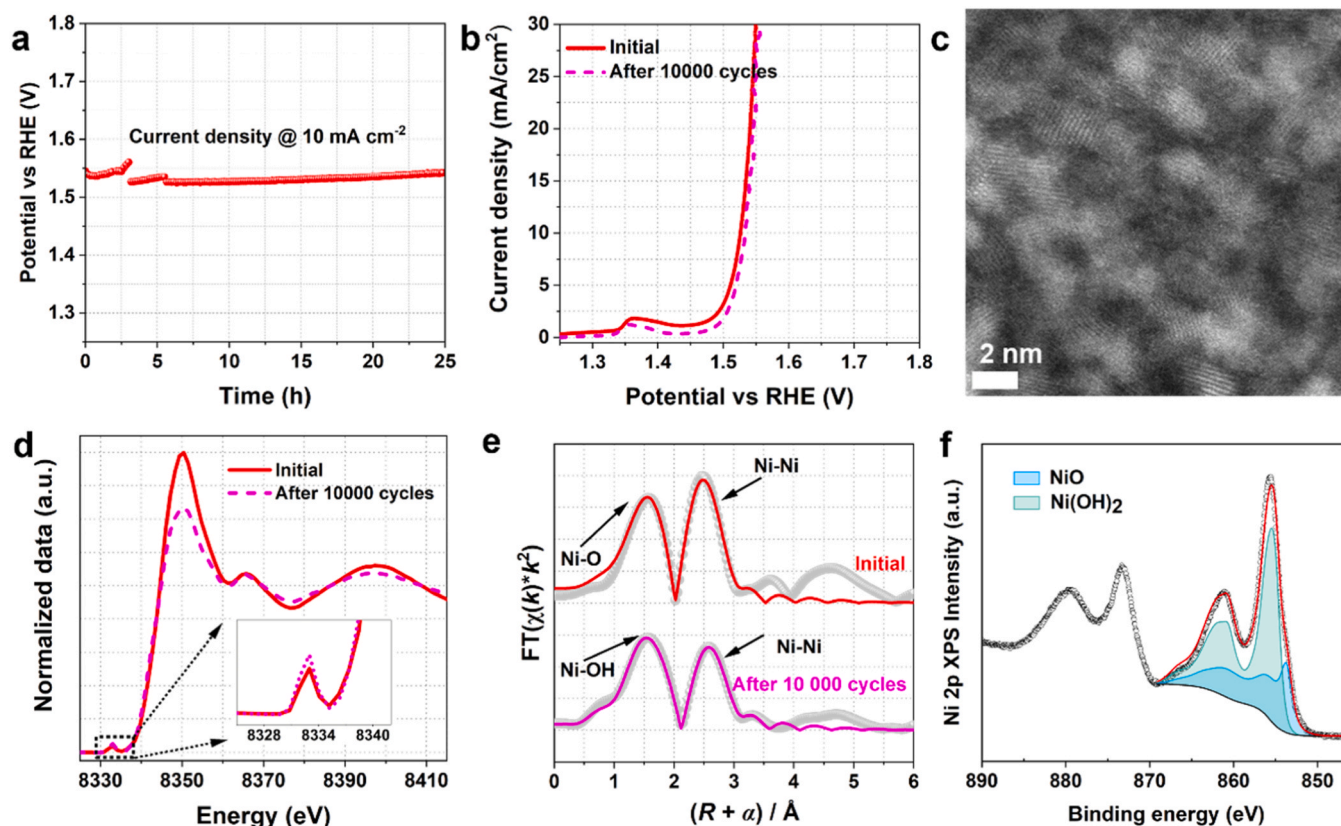


**Fig. 4.** Stability test of NiO dots/a-carbon. a) Time-dependent potential curve of NiO dots/a-carbon at the current density of  $10 \text{ mA cm}^{-2}$ . b) The OER polarization curves of NiO dots/a-carbon before (solid) and after (dot) accelerated deterioration tests (ADT). c) A HR-TEM of NiO dots/a-carbon after the ADT. d) The Ni K-edge XANES spectra of NiO dots/a-carbon before (solid) and after (dot) the ADT. e) The  $k^2$ -weighted  $\chi(k)$ -function of the EXAFS spectra of NiO dots/a-carbon and NiO dots/a-carbon after the ADT. f) Ni 2p XPS of NiO dots/a-carbon after ADT.

electrocatalyst shows significant voltage loss after the ADT in Fig. S19. A sequence of measurements, including HR-TEM, XAS and XPS, were further conducted for the NiO dots/a-carbon after the durability test. The HR-TEM image (Fig. 4c) and the statistical analysis (Fig. S20) reveal that the size of NiO quantum dots increase slightly. The Ni K-edge of NiO dots/a-carbon before and after the ADT test in the XANES spectra are nearly overlapping in Fig. 4e, suggesting that the high-valence state of Ni is sustained. The observed reduction in white line intensity after the ADT test indicates changes in the local environment of Ni atoms, which can be attributed to changes in the ligand field of Ni atoms from NiO into NiOOH or Ni(OH)<sub>2</sub> [66]. The increase in the pre-edge peak intensity implies that the local environment of the Ni atoms has become more distorted or asymmetric. This distortion is plausibly due to the evolution of OH groups, which have different electronic and structural properties. The changed ligand field is confirmed by the EXAFS fitting and Ni 2p XPS analysis. The EXAFS fitting was implemented with Ni-OH and Ni-Ni paths for NiO dots/a-carbon after 10 000 cycles. As shown by the fitting parameters in Table S5, the coordination number of Ni-OH ( $N_{\text{Ni-O}}$ ) and Ni-Ni ( $N_{\text{Ni-Ni}}$ ) are 4.0 and 3.9, respectively, indicate a disordered structure. The amount of Ni(OH)<sub>2</sub> is estimated to be 67 % in the Ni 2p XPS in Fig. 4f. The O 1s spectra in Fig. S21 clearly shows a peak at 531.3 eV, which can be attribute to the Ni(OH)<sub>2</sub>. It should be noted that the peak shape and position are almost the same for NiOOH and Ni(OH)<sub>2</sub>, and they cannot be really discerned. The excellent electrochemical durability can be attributed to the strong interaction between the NiO quantum dots and the functional groups on amorphous carbon, which significantly prevents the aggregation and liberation of NiO.

### 3.4. Water electrolyzer performance of NiO dots/a-carbon

The OER activity experimentally investigated on an AEMEL cell with a sandwiched structure of NiO dots/a-carbon (anode) | FAA-3-30 membrane | 40 wt% Pt, 40 wt% Ru, 20 wt% C (cathode). The AEMEL experiments were performed in a 0.1 M KOH solution at 45 °C. Fig. 5a shows a schematic picture of the membrane electrode assembly (MEA) fabricated for the NiO dots/a-carbon anode of the AEMEL cell, in which the liquid alkaline electrolyte is circulated through the electrodes and separated by the ion exchange membrane. Photos of the cell are shown in Fig. S22. To maximize electrolyzer performance based on NiO dots/a-carbon, the influence of catalyst loading was investigated at the same conditions. Improvements in the performance are achieved by increasing the catalysts loading from 1.1 to 2.9 mg cm<sup>-2</sup> as shown in Fig. 5b. However, further increase in the loading leads to a decrease of the MEA activity (Fig. S23), because ohmic and mass transfer losses dominate in the thick electrode and an increasing number of active sites cannot compensate for that [67,68].

The NiO dots/a-carbon MEA performance is compared with the one obtained when using the commercial RuO<sub>2</sub> anode with the same loading in Fig. 5c. In the kinetic region, that is, at cell voltages of less than 1.58 V, the NiO dots/a-carbon MEA shows a small onset overpotential of 228 mV (defined by current density of  $10 \text{ mA cm}^{-2}$ ), which is 46 mV smaller than that of the commercial RuO<sub>2</sub> based MEA. At a cell voltage of 1.55 V, the NiO dots/a-carbon MEA delivers a current density of  $67 \text{ mA cm}^{-2}$  (Fig. S24), which is more than twice the one obtained with the commercial RuO<sub>2</sub> MEA ( $29 \text{ mA cm}^{-2}$ ). Detailed comparisons of overpotentials at selected current densities (from  $10 \text{ mA cm}^{-2}$  to  $300 \text{ mA cm}^{-2}$ ) are shown in Fig. 5d. A current density of  $500 \text{ mA cm}^{-2}$  is obtained at 1.708 V for NiO dots/a-carbon at 45 °C and the

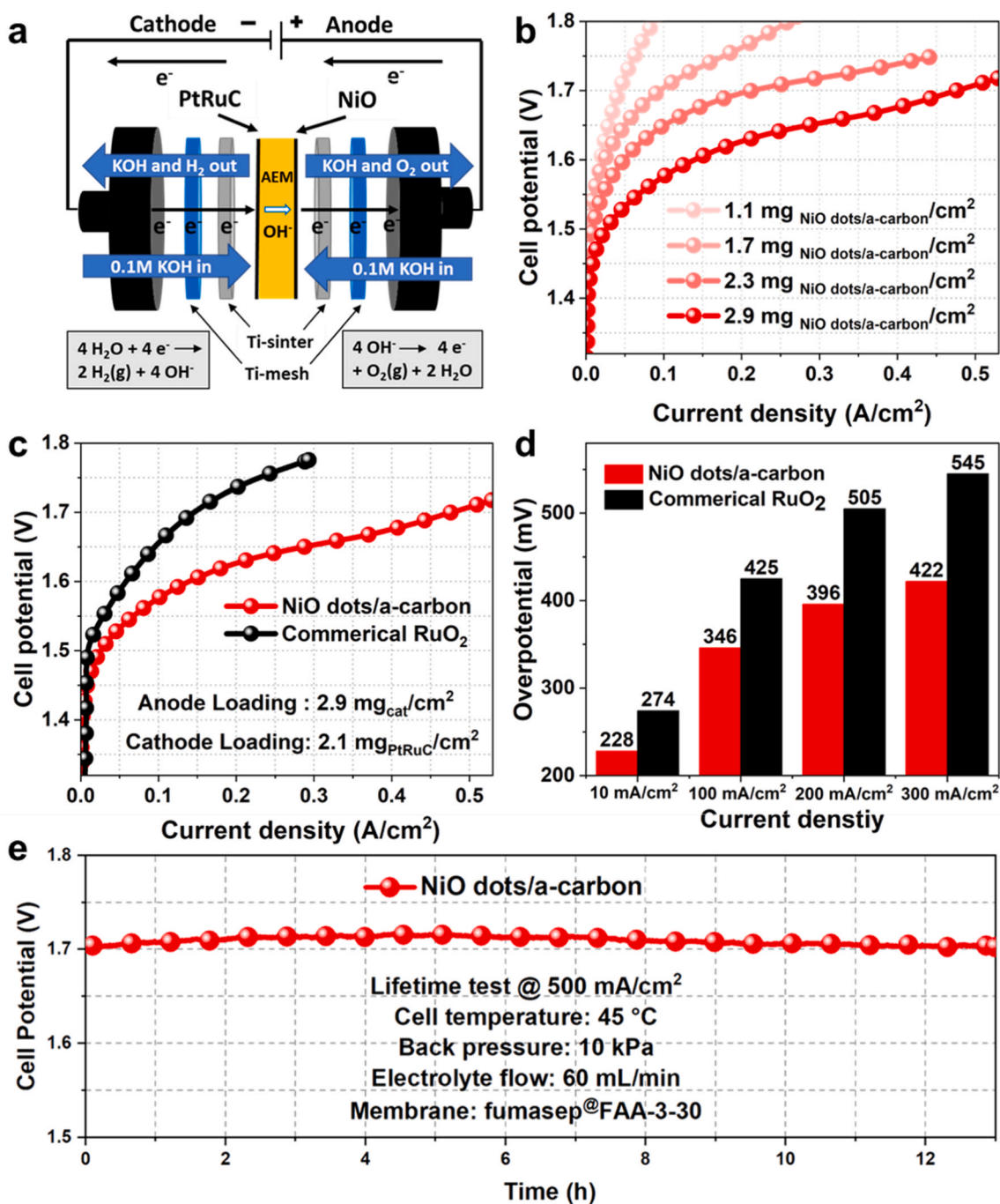


**Fig. 5.** Water electrolyzer performance of NiO dots/a-carbon. a) A schematic picture of the AEMEL cell. b) Current-voltage profiles of the NiO dots/a-carbon catalyst MEAs with different mass loadings. c) Current-voltage profiles of the NiO dots/a-carbon and RuO<sub>2</sub> MEAs in 0.1 M KOH. The voltage is ohmic resistance-free. d) Overpotentials of the NiO dots/a-carbon and the commercial RuO<sub>2</sub> MEAs at different current densities. e) The time-dependent cell potential curve of the NiO dots/a-carbon MEA at the current density of 500 mA cm<sup>-2</sup>.

performance loss is negligible after a 12 h stability test (Fig. 5e) at such high current density, indicating its great potential in practical applications at a high current density. The MEA performance is compared with reported literature in Table S6, suggesting a superior water splitting activity [69–76]. EIS measurements in Fig. S25 show the excellent performance of NiO dots/a-carbon and the lower overall loss of the NiO dots/a-carbon MEA. However, because the time constants of various electrochemical processes overlap, the contributions from various loss mechanisms cannot be identified by fitting the full cell-impedance spectrum.

### 3.5. DFT calculations

Density functional theory (DFT) calculations were also performed to understand the enhanced OER activity of NiO dots/a-carbon. The computational details are given in the supporting information (Table S7). Despite XPS suggests association of Ni<sup>δ+</sup> (2 < δ < 3) with β-NiOOH, the latter is not used in DFT as a model surface because our experimental findings do not indisputably confirm its presence. The (200) plane of NiO is considered as the model catalyst surface since it is the most exposed surface based on the experimental XRD pattern in Fig. S26. Considering that the promoted Ni valence state is induced by

an electron-withdrawing effect of the oxygen functional groups, one electron is removed from the NiO (200) facet to simulate the low electronic density on the surface of NiO dots/a-carbon. The standard cubic NiO model was established to simulate nanocrystalline NiO. The density of states is shown in Fig. S27. The band gap of 2.17 eV for cubic NiO predicted at the DFT + U level with  $U - J = 5.77$  eV agrees well with the experimental value of 2.30 eV, where  $U$  is the on-site Coulomb term and  $J$  is the site exchange term [77]. When one electron is removed from the (200) plane, the hole is redistributed over the whole surface. According to the Bader population analysis, the average charge of the Ni atoms of the (200) surface of nanocrystalline NiO is 1.01  $e$  and 1.03  $e$  for the NiO dots/a-carbon [78,79]. Although the atomic charges change only slightly, the hole density increases significantly as seen in the middle of the differential charge density in Fig. 6a. The hole at the electron cloud of the Ni atom may enable a more efficient charge transfer during the catalytic process.

The Gibbs free-energy profile and the adsorbed intermediates of the OER reaction steps are shown in Fig. 6b and Fig. S28, respectively. The calculations suggest that the adsorption reaction of OH on the surface from the solution is exergonic and the endergonic formation of  $^*O$  has a reaction energy of only 0.20 eV for the 200 facet of NiO in NiO dots/a-carbon, whereas the reaction free energy of 0.23 eV for nanocrystalline NiO is slightly larger. The subsequent formation of  $^*OOH$  is exergonic with a free energy of 2.27 eV for NiO dots/a-carbon as compared to 2.42 eV for nanocrystalline NiO. The last reaction step, that is, the formation of  $O_2$  and  $H_2O$ , is endergonic with a free energy of 3.19 eV, which is slightly smaller than reaction free energy of 3.28 eV for nanocrystalline NiO. The last step is the potential-determining step for the oxygen evolution reaction because it has the largest reaction energy. The DFT analysis supports the experimental findings, which indicate that the high-valent  $Ni^{\delta+}$  ( $2 < \delta < 3$ ) improve the OER catalytic activity,

owing to the lower barrier for the generation of  $^*O$  and  $^*OH$  intermediates.

#### 4. Discussion

In summary, NiO quantum dots uniformly distributed on amorphous carbon were successfully prepared and further applied for alkaline water electrolysis. We demonstrate that the amorphous carbon-induced Ni valence state modulation can significantly improve the OER performance of NiO quantum dots. XPS and XAS analysis reveal that amorphous carbon accommodates oxygen functional groups, which are beneficial for promoting the valence state of Ni. The promoted  $Ni^{\delta+}$  ( $2 < \delta < 3$ ) increase the electron hole intensity in NiO, enabling efficient charge transfer during the OER as concluded from the DFT calculations. Moreover, the tiny size of NiO dots enables a greater metal utilization, and the open 2D amorphous carbon prevents the aggregation of NiO dots during OER processes. The high-valent NiO dots/a-carbon electrocatalyst show enhancement in OER activity, compared with nanocrystalline NiO, while a small degradation of 7 mV after 10 000 ADT cycles is observed in the RDE measurement. A current density of 500  $mA\ cm^{-2}$  at 1.708 V was achieved in the AEMEL measurements at 45 °C and the cell voltage loss is negligible when the current density of 500  $mA\ cm^{-2}$  is conducted for more than 12 h. This work provides a deeper understanding of the design and construction of high-valent Ni electrocatalysts for efficient water electrolysis.

#### CRedit authorship contribution statement

**Tanja M. Kallio:** Writing – review & editing, Validation, Supervision, Resources, Project administration, Funding acquisition, Conceptualization. **Benjin Jin:** Writing – original draft, Visualization,

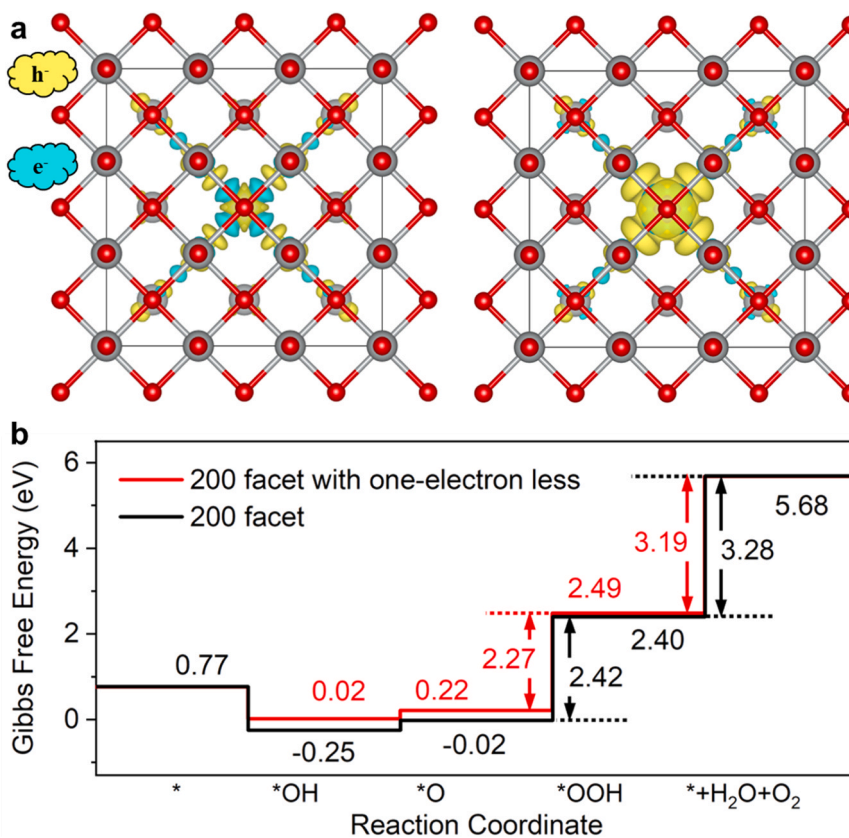


**Fig. 6.** DFT calculations of NiO with high valence state. a) The simulated charge distribution of the (200) plane of neutral NiO (left) and of oxidized NiO (right). b) The Gibbs free-energy diagram for the OER reaction steps on the (200) plane. The black lines represent the reaction steps on neutral NiO, whereas the red ones are for the reactions on the oxidized (200) plane.

Methodology, Investigation, Formal analysis, Conceptualization. **Nana Han:** Writing – review & editing, Supervision, Conceptualization. **Dage Sundholm:** Writing – review & editing, Supervision, Methodology. **Simo J Huotari:** Writing – review & editing, Investigation. **Antti-Jussi Kallio:** Investigation. **Basit Ali:** Writing – review & editing. **Junjie Shi:** Writing – review & editing, Investigation. **Hua Jiang:** Writing – review & editing, Investigation. **Viktoriia A. Saveleva:** Writing – review & editing, Investigation, Formal analysis. **Jani Sainio:** Writing – original draft, Investigation, Formal analysis. **Qian Wang:** Writing – original draft, Visualization, Investigation, Formal analysis.

## Declaration of Competing Interest

The authors declare that they have no known competing financial interests or personal relationships that could have appeared to influence the work reported in this paper.

## Data Availability

Data will be made available on request.

## Acknowledgment

We acknowledge the facilities provided by Aalto University OtaNano - Nanomicroscopy Center (Aalto-NMC), BIOECONOMY, and RAMI infrastructures. This project has received funding from the European Union's Horizon 2020 research and innovation programme under grant agreement No 952068 (HydrogenLung) and No. 892856 (LESGO). We thank Research Council of Finland (the Profi 7 project, No. 352955) for financial support. This work has also been supported by Research Council of Finland through project 340583. QW thanks the China Scholarship Council for a pre-doctoral fellowship. Computational resources from the CSC – IT Center for Science, Finland are acknowledged. We acknowledge the European Synchrotron Radiation Facility (ESRF) for provision of synchrotron radiation facilities under proposal number CH6530 (DOI /10.15151/ESRF-ES-962082917). We acknowledge the Helsinki Center for X-ray Spectroscopy for providing experiment time and support with the Hel-XAS spectrometer under proposal number 2022–0012.

## Supplemental information

Document S1 is the main supplemental PDF.

## Appendix A. Supporting information

Supplementary data associated with this article can be found in the online version at [doi:10.1016/j.apcatb.2024.124437](https://doi.org/10.1016/j.apcatb.2024.124437).

## References

- R. Abbasi, B.P. Setzler, S. Lin, J. Wang, Y. Zhao, H. Xu, B. Pivovar, B. Tian, X. Chen, G. Wu, Y. Yan, A roadmap to low-cost hydrogen with hydroxide exchange membrane electrolyzers, *Adv. Mater.* 31 (2019) e1805876.
- T. ul Haq, Y. Haik, A roadmap towards sustainable anode design for alkaline water electrolysis, *Appl. Catal. B Environ.* 334 (2023).
- I. Vincent, D. Bessarabov, Low cost hydrogen production by anion exchange membrane electrolysis: a review, *Renew. Sust. Energy Rev.* 81 (2018) 1690–1704.
- J.Q. Shan, C.X. Guo, Y.H. Zhu, S.M. Chen, L. Song, M. Jaroniec, Y. Zheng, S.Z. Qiao, Charge-Redistribution-enhanced nanocrystalline Ru@IrOx electrocatalysts for oxygen evolution in acidic media, *Chem. Us* 5 (2019) 445–459.
- K.E. Ayers, E.B. Anderson, C.B. Capuano, M. Niedzweicki, M. Hickner, C.Y. Wang, Y. Len, W. Zhou, Characterization of anion exchange membrane technology for low cost electrolysis, *Ecs Trans.* 45 (2013) 121–130.
- A. Buttler, H. Spliethoff, Current status of water electrolysis for energy storage, grid balancing and sector coupling via power-to-gas and power-to-liquids: a review, *Renew. Sust. Energy Rev.* 82 (2018) 2440–2454.
- L. Guo, J. Xie, S.Y. Chen, Z.X. He, Y.Z. Liu, C.X. Shi, R.J. Gao, L. Pan, Z.F. Huang, X. W. Zhang, J.J. Zou, Self-supported crystalline-amorphous composites of metal phosphate and NiS for high-performance water electrolysis under industrial conditions, *Appl. Catal. B Environ.* 340 (2024).
- J. Brauns, T. Turek, Alkaline water electrolysis powered by renewable energy: a review, *Processes* 8 (2) (2020) 248.
- E. Gulzow, Alkaline fuel cells: a critical view, *J. Power Sources* 61 (1996) 99–104.
- C.Q. Li, J.B. Baek, The promise of hydrogen production from alkaline anion exchange membrane electrolyzers, *Nano Energy* 87 (2021).
- G.H. Choi, N.C.S. Selvam, H. Kim, Y.S. Park, J. Jung, M. Gyun, H.S. Jeon, A.S. Lee, W.S. Yoon, P.J. Yoo, High-valent metal site incorporated heterointerface catalysts for high-performance anion-exchange membrane water electrolyzers, *Appl. Catal. B Environ.* 333 (2023).
- X.X. Zou, Y.Y. Wu, Y.P. Liu, D.P. Liu, W. Li, L. Gu, H. Liu, P.W. Wang, L. Sun, Y. Zhang, Generation of bifunctional, efficient Fe-based catalysts from mackinawite iron sulfide for water splitting, *Chem. Us* 4 (2018) 1139–1152.
- J.X. Kang, X.Y. Qiu, Q. Hu, J. Zhong, X. Gao, R. Huang, C.Z. Wan, L.M. Liu, X. F. Duan, L. Guo, Valence oscillation and dynamic active sites in monolayer NiCo hydroxides for water oxidation, *Nat. Catal.* 4 (2021) 1050–1058.
- L. Li, X. Cao, J. Huo, J. Qu, W. Chen, C. Liu, Y. Zhao, H. Liu, G. Wang, High valence metals engineering strategies of Fe/Co/Ni-based catalysts for boosted OER electrocatalysis, *J. Energy Chem.* 76 (2023) 195–213.
- R.D. Smith, C.P. Berlinguette, Accounting for the dynamic oxidative behavior of nickel anodes, *J. Am. Chem. Soc.* 138 (2016) 1561–1567.
- D.K. Bediako, B. Lassalle-Kaiser, Y. Surendranath, J. Yano, V.K. Yachandra, D. G. Nocera, Structure-activity correlations in a nickel-borate oxygen evolution catalyst, *J. Am. Chem. Soc.* 134 (2012) 6801–6809.
- M. Han, N. Wang, B. Zhang, Y.J. Xia, J. Li, J.R. Han, K.L. Yao, C.C. Gao, C.N. He, Y. C. Liu, Z.M. Wang, A. Seifitokaldani, X.H. Sun, H.Y. Liang, High-valent nickel promoted by atomically embedded copper for efficient water oxidation, *Acc Catal.* 10 (2020) 9725–9734.
- J.Y. Chen, L. Dang, H. Liang, W. Bi, J.B. Gerken, S. Jin, E.E. Alp, S.S. Stahl, Operando analysis of NiFe and Fe oxyhydroxide electrocatalysts for water oxidation: detection of Fe(4)(+) by Mossbauer spectroscopy, *J. Am. Chem. Soc.* 137 (2015) 15090–15093.
- I.C. Gerber, P. Serp, A theory/experience description of support effects in carbon-supported catalysts, *Chem. Rev.* 120 (2020) 1250–1349.
- Y.C. Yang, Y.W. Yang, Z.X. Pei, K.H. Wu, C.H. Tan, H.Z. Wang, L. Wei, A. Mahmood, C. Yan, J.C. Dong, S.L. Zhao, Y. Chen, Recent progress of carbon-supported single-atom catalysts for energy conversion and storage, *Matter-Us* 3 (2020) 1442–1476.
- M.Y. Ma, H.Z. Yu, L.M. Deng, L.Q. Wang, S.Y. Liu, H. Pan, J.W. Ren, M. Y. Maximov, F. Hu, S.J. Peng, Interfacial engineering of heterostructured carbon-supported molybdenum cobalt sulfides for efficient overall water splitting, *Tungsten-Singap.* 5 (2023) 589–597.
- J. Wang, K. Li, H.X. Zhong, D. Xu, Z.L. Wang, Z. Jiang, Z.J. Wu, X.B. Zhang, Synergistic effect between metal-nitrogen-carbon sheets and NiO nanoparticles for enhanced electrochemical water-oxidation performance, *Angew. Chem. Int. Ed. Engl.* 54 (2015) 10530–10534.
- Y. Liang, Y. Li, H. Wang, J. Zhou, J. Wang, T. Regier, H. Dai, Co(3)O(4) nanocrystals on graphene as a synergistic catalyst for oxygen reduction reaction, *Nat. Mater.* 10 (2011) 780–786.
- G. Wu, X.S. Zheng, P.X. Cui, H.Y. Jiang, X.Q. Wang, Y.T. Qu, W.X. Chen, Y. Lin, H. Li, X. Han, Y.M. Hu, P.G. Liu, Q.H. Zhang, J.J. Ge, Y.C. Yao, R.B. Sun, Y. Wu, L. Gu, X. Hong, Y.D. Li, A general synthesis approach for amorphous noble metal nanosheets, *Nat. Commun.* 10 (2019).
- R.L. Li, S.K. Yang, Y.D. Zhang, G. Yu, C. Wang, C. Chen, G. Wu, R.B. Sun, G. Z. Wang, X.S. Zheng, W.S. Yan, G.M. Wang, D.W. Rao, X. Hong, Short-range order in amorphous nickel oxide nanosheets enables selective and efficient electrochemical hydrogen peroxide production, *Cell Rep. Phys. Sci.* 3 (2022).
- M.C. Biesinger, B.P. Payne, L.W.M. Lau, A. Gerson, R.S.C. Smart, X-ray photoelectron spectroscopic chemical state quantification of mixed nickel metal, oxide and hydroxide systems, *Surf. Interface Anal.* 41 (2009) 324–332.
- I.S. Filimonenkov, S.Y. Istomin, E.V. Antipov, G.A. Tsirlina, E.R. Savinova, Rotating ring-disk electrode as a quantitative tool for the investigation of the oxygen evolution reaction, *Electro Acta* 286 (2018) 304–312.
- J.P. Perdew, J.A. Chevary, S.H. Vosko, K.A. Jackson, M.R. Pederson, D.J. Singh, C. Fiolhais, Atoms, molecules, solids, and surfaces - applications of the generalized gradient approximation for exchange and correlation (Vol 46, Pg 6671, 1992), *Phys. Rev. B* 48 (1993) 4978–49718.
- O. Bengone, M. Alouani, P. Blöchl, J. Hugel, Implementation of the projector augmented-wave LDA+U method: application to the electronic structure of NiO, *Phys. Rev. B* 62 (2000) 16392–16401.
- V.I. Anisimov, A.I. Poteryaev, M.A. Korotin, A.O. Anokhin, G. Kotliar, First-principles calculations of the electronic structure and spectra of strongly correlated systems: dynamical mean-field theory, *J. Phys. Condens. Mat.* 9 (1997) 7359–7367.
- J.P. Perdew, K. Burke, M. Ernzerhof, Generalized gradient approximation made simple, *Phys. Rev. Lett.* 77 (1996) 3865–3868.
- P.E. Blochl, Projector augmented-wave method, *Phys. Rev. B* 50 (1994) 17953–17979.
- G. Kresse, D. Joubert, From ultrasoft pseudopotentials to the projector augmented-wave method, *Phys. Rev. B* 59 (1999) 1758–1775.
- S.L. Dudarev, G.A. Botton, S.Y. Savrasov, C.J. Humphreys, A.P. Sutton, Electron-energy-loss spectra and the structural stability of nickel oxide: an LSDA+U study, *Phys. Rev. B* 57 (1998) 1505–1509.
- R. Long, N.J. English, D.A. Mooney, Electronic structures of N- and C-doped NiO from first-principles calculations, *Phys. Lett. A* 374 (2010) 1184–1187.

- [36] A. Rohrbach, J. Hafner, G. Kresse, Molecular adsorption on the surface of strongly correlated transition-metal oxides: a case study for CO/NiO(100), *Phys. Rev. B* (69) (2004).
- [37] S. Grimme, J. Antony, S. Ehrlich, H. Krieg, A consistent and accurate ab initio parametrization of density functional dispersion correction (DFT-D) for the 94 elements H-Pu, *J. Chem. Phys.* 132 (2010).
- [38] S.H. Hong, J. Winter, Micro-Raman spectroscopy on C:H nanoparticles: art. no. 124304, *J. Appl. Phys.* 98 (2005) 124304.
- [39] Y.M. Hu, M.Z. Zhu, X. Luo, G. Wu, T.T. Chao, Y.T. Qu, F.Y. Zhou, R.B. Sun, X. Han, H. Li, B. Jiang, Y. Wu, X. Hong, Coplanar Pt/C nanomeshes with ultrastable oxygen reduction performance in fuel cells, *Angew. Chem. Int. Ed.* 60 (2021) 6533–6538.
- [40] M.C. Biesinger, *X-ray Photoelectron Spectroscopy (XPS) Reference Pages*, 1981.
- [41] Z. Cai, L. Li, Y. Zhang, Z. Yang, J. Yang, Y. Guo, L. Guo, Amorphous nanocages of Cu-Ni-Fe Hydr(oxy)oxide prepared by photocorrosion for highly efficient oxygen, *Evol., Angew. Chem. Int. Ed. Engl.* 58 (2019) 4189–4194.
- [42] X. Su, Y. Wang, J. Zhou, S. Gu, J. Li, S. Zhang, Operando spectroscopic identification of active sites in NiFe prussian blue analogues as electrocatalysts: activation of oxygen atoms for oxygen evolution reaction, *J. Am. Chem. Soc.* 140 (2018) 11286–11292.
- [43] T.I.T. Okpalugo, P. Papakonstantinou, H. Murphy, J. McLaughlin, N.M.D. Brown, High resolution XPS characterization of chemical functionalised MWCNTs and SWCNTs, *Carbon* 43 (2005) 153–161.
- [44] L.G. Thygesen, M.M. Lokke, E. Micklander, S.B. Engelsen, Vibrational microspectroscopy of food. Raman vs. FT-IR, *Trends Food Sci. Technol.* 14 (2003) 50–57.
- [45] C. Gougoussis, M. Calandra, A. Seitsonen, C. Brouder, A. Shukla, F. Mauri, Intrinsic charge transfer gap in NiO from Ni K-edge x-ray absorption spectroscopy, *Phys. Rev. B* 79 (2009).
- [46] Y.R. Denny, K. Takahashi, K. Niki, D.S. Yang, T. Fujikawa, H.J. Kang, Ni K-edge XAFS analysis of NiO thin film with multiple scattering theory, *Surf. Interface Anal.* 46 (2014) 997–999.
- [47] T. Yamamoto, Assignment of pre-edge peaks in K-edge x-ray absorption spectra of 3d transition metal compounds: electric dipole or quadrupole? *X-Ray Spectrom.* 37 (2008) 572–584.
- [48] J. Zaenen, G.A. Sawatzky, J.W. Allen, Band gaps and electronic structure of transition-metal compounds, *Phys. Rev. Lett.* 55 (1985) 418–421.
- [49] H. Liu, Q. He, H. Jiang, Y. Lin, Y. Zhang, M. Habib, S. Chen, L. Song, Electronic structure reconfiguration toward pyrite NiS(2) via engineered heteroatom defect boosting overall water splitting, *ACS Nano* 11 (2017) 11574–11583.
- [50] U. Boesenberg, M.A. Marcus, A.K. Shukla, T. Yi, E. McDermott, P.F. Teh, M. Srinivasan, A. Moewes, J. Cabana, Asymmetric pathways in the electrochemical conversion reaction of NiO as battery electrode with high storage capacity, *Sci. Rep.* 4 (2014) 7133.
- [51] M. Jafarian, M. Babae, F. Gobal, M.G. Mahjani, Electro-oxidation of alcohols on nickel dispersed in poly-o-aminophenol modified graphite electrode, *J. Electrochem.* 652 (2011) 8–12.
- [52] L. Negahdar, F. Zeng, S. Palkovits, C. Broicher, R. Palkovits, Mechanistic aspects of the electrocatalytic oxygen evolution reaction over Ni-Co oxides, *Chemelectrochem* 6 (2019) 5588–5595.
- [53] Y. Bu, O. Gwon, G. Nam, H. Jang, S. Kim, Q. Zhong, J. Cho, G. Kim, A highly efficient and robust cation ordered perovskite oxide as a bifunctional catalyst for rechargeable zinc-air batteries, *ACS Nano* 11 (2017) 11594–11601.
- [54] B. Hua, M. Li, J.L. Luo, A facile surface chemistry approach to bifunctional excellence for perovskite electrocatalysis, *Nano Energy* 49 (2018) 117–125.
- [55] Z. Zhang, B. He, L. Chen, H. Wang, R. Wang, L. Zhao, Y. Gong, Boosting overall water splitting via FeOOH nanoflake-decorated PrBa(0.5)Sr(0.5)Co(2)O(5+delta) nanorods, *ACS Appl. Mater. Interfaces* 10 (2018) 38032–38041.
- [56] Y.F. Bu, H. Jang, O. Gwon, S.H. Kim, S.H. Joo, G. Nam, S. Kim, Y. Qin, Q. Zhong, S. K. Kwak, J. Cho, G. Kim, Synergistic interaction of perovskite oxides and N-doped graphene in versatile electrocatalyst, *J. Mater. Chem. A* 7 (2019) 2048–2054.
- [57] V. Hoang, K.N. Dinh, V.G. Gomes, Hybrid Ni/NiO composite with N-doped activated carbon from waste cauliflower leaves: a sustainable bifunctional electrocatalyst for efficient water splitting, *Carbon* 157 (2020) 515–524.
- [58] V.C. Hoang, V.G. Gomes, K.N. Dinh, Ni- and P-doped carbon from waste biomass: a sustainable multifunctional electrode for oxygen reduction, oxygen evolution and hydrogen evolution reactions, *Electro Acta* 314 (2019) 49–60.
- [59] J. He, M. Wang, W. Wang, R. Miao, W. Zhong, S.Y. Chen, S. Poges, T. Jafari, W. Song, J. Liu, S.L. Suib, Hierarchical mesoporous NiO/MnO(2)@PANI core-shell microspheres, highly efficient and stable bifunctional electrocatalysts for oxygen evolution and reduction reactions, *ACS Appl. Mater. Interfaces* 9 (2017) 42676–42687.
- [60] Q. Li, J.B. Wu, T. Wu, H.R. Jin, N. Zhang, J. Li, W.X. Liang, M.L. Liu, L. Huang, J. Zhou, Phase engineering of atomically thin perovskite oxide for highly active oxygen evolution, *Adv. Funct. Mater.* 31 (2021).
- [61] S.M. Pawar, B.S. Pawar, B. Hou, J. Kim, A.T.A. Ahmed, H.S. Chavan, Y. Jo, S. Cho, A.I. Inamdar, J.L. Gunjekar, H. Kim, S. Cha, H. Im, Self-assembled two-dimensional copper oxide nanosheet bundles as an efficient oxygen evolution reaction (OER) electrocatalyst for water splitting applications, *J. Mater. Chem. A* 5 (2017) 12747–12751.
- [62] Y. Zhu, W. Zhou, Y. Chen, J. Yu, M. Liu, Z. Shao, A. High-Performance, Electrocatalyst for oxygen evolution reaction: LiCo<sub>0.8</sub>Fe<sub>0.2</sub>O<sub>2</sub>, *Adv. Mater.* 27 (2015) 7150–7155.
- [63] L. Fan, E.L. Rautama, J. Lindén, J. Sainio, H. Jiang, O. Sorsa, N. Han, C. Flox, Y. Zhao, Y. Li, T. Kallio, Two orders of magnitude enhancement in oxygen evolution reactivity of La<sub>0.7</sub>Sr<sub>0.3</sub>Fe<sub>1</sub>-Ni O<sub>3</sub>- by improving the electrical conductivity, *Nano Energy* 93 (2022).
- [64] A.R.C. Bredar, A.L. Chown, A.R. Burton, B.H. Farnum, Electrochemical impedance spectroscopy of metal oxide electrodes for energy applications, *ACS Appl. Energ. Mater.* 3 (2020) 66–98.
- [65] L.P. Korniienko, V.E. Kasatkin, A.I. Scherbakov, I.G. Korosteleva, I.V. Kasatkina, V. N. Dorofeeva, Electrochemical studies of the state of a nickel surface in an alkaline medium, *Prot. Met Phys. Chem. +* 58 (2022) 1213–1219.
- [66] T. Sakamoto, H. Kishi, S. Yamaguchi, D. Matsumura, K. Tamura, A. Hori, Y. Horiuchi, A. Serov, K. Artyushkova, P. Atanassov, H. Tanaka, Mechanism study of hydrazine electrooxidation reaction on nickel oxide surface in alkaline electrolyte by in situ XAFS, *J. Electrochem Soc.* 163 (2016) H951–H957.
- [67] O. Sorsa, R. Backhouse, S. Saxelin, T. Rajala, H. Jiang, P. Kauranen, T. Kallio, Optimization and aging of Pt nanowires supported on single-walled carbon nanotubes as a cathode catalyst in polymer electrolyte membrane water electrolyser, *Int J. Hydrog. Energ.* 45 (2020) 19121–19132.
- [68] S.A. Grigoriev, A.A. Kalinnikov, Mathematical modeling and experimental study of the performance of PEM water electrolysis cell with different loadings of platinum metals in electrocatalytic layers, *Int J. Hydrog. Energ.* 42 (2017) 1590–1597.
- [69] Y.S. Park, J. Yang, J. Lee, M.J. Jang, J. Jeong, W.S. Choi, Y. Kim, Y.D. Yin, M. H. Seo, Z.W. Chen, S.M. Choi, Superior performance of anion exchange membrane water electrolyzer: ensemble of producing oxygen vacancies and controlling mass transfer resistance, *Appl. Catal. B Environ.* (278) (2020).
- [70] T. Pandiarajan, L.J. Berchmans, S. Ravichandran, Fabrication of spinel ferrite based alkaline anion exchange membrane water electrolyzers for hydrogen production, *RSC Adv.* 5 (2015) 34100–34108.
- [71] C.C. Pavel, F. Cecconi, C. Emiliani, S. Santiccioli, A. Scaffidi, S. Catanorchi, M. Comotti, Highly efficient platinum group metal free based membrane-electrode assembly for anion exchange membrane water electrolysis, *Angew. Chem. Int. Ed.* 53 (2014) 1378–1381.
- [72] E. López-Fernández, J. Gil-Rostra, J.P. Espinós, A.R. González-Elipe, F. Yubero, A. de Lucas-Consuegra, CuCo<sub>3</sub>-xO<sub>4</sub> ultra-thin film as efficient anodic catalysts for anion exchange membrane water electrolyzers, *J. Power Sources* 415 (2019) 136–144.
- [73] L. Zeng, T.S. Zhao, R.H. Zhang, J.B. Xu, NiCo<sub>2</sub>O<sub>4</sub> nanowires@MnOx nanoflakes supported on stainless steel mesh with superior electrocatalytic performance for anion exchange membrane water splitting, *Electrochem Commun.* 87 (2018) 66–70.
- [74] L. Xiao, S. Zhang, J. Pan, C.X. Yang, M.L. He, L. Zhuang, J.T. Lu, First implementation of alkaline polymer electrolyte water electrolysis working only with pure water, *Energ. Environ. Sci.* 5 (2012) 7869–7871.
- [75] D.Y. Xu, M.B. Stevens, M.R. Cosby, S.Z. Oener, A.M. Smith, L.J. Enman, K.E. Ayers, C.B. Capuano, J.N. Renner, N. Danilovic, Y.G. Li, H.Z. Wang, Q.H. Zhang, S. W. Boettcher, Earth-abundant oxygen electrocatalysts for alkaline anion-exchange-membrane water electrolysis: effects of catalyst conductivity and comparison with performance in three-electrode cells, *ACS Catal.* 9 (2019) 7–15.
- [76] B.K. Kakati, D. Sathiyamoorthy, A. Verma, Electrochemical and mechanical behavior of carbon composite bipolar plate for fuel cell, *Int J. Hydrog. Energ.* 35 (2010) 4185–4194.
- [77] Data Retrieved from the Materials Project for NiO (mp-19009) from Database Version v2022.10.28.
- [78] W. Tang, E. Sanville, G. Henkelman, A grid-based Bader analysis algorithm without lattice bias, *J. Phys. Condens Matter* 21 (2009) 084204.
- [79] E. Sanville, S.D. Kenny, R. Smith, G. Henkelman, Improved grid-based algorithm for Bader charge allocation, *J. Comput. Chem.* 28 (2007) 899–908.